

Valery I. Levitas^a, Mahdi Javanbakht^b

^aIowa State University, Departments of Aerospace Engineering, Mechanical Engineering, and Material Science and Engineering, Ames, Iowa, U.S.A.

^bIowa State University, Department of Mechanical Engineering, Ames, Iowa, U.S.A.

Phase-field approach to martensitic phase transformations: Effect of martensite–martensite interface energy

Dedicated to Prof. F. D. Fischer on the occasion of his 70th birthday

A generalization of the phase-field theory for multivariant martensitic phase transformations is suggested that allows one to vary martensite–martensite interface energy independent of energy for austenite–martensite interfaces. The finite element method is utilized to solve the coupled phase-field and elasticity equations. Width and energy of the austenite–martensite interfaces are determined. Splitting of the martensite–martensite interface into two austenite–martensite interfaces, leading to barrierless austenite nucleation, is obtained. The effect of the martensite–martensite interface energy and grain size on the stationary and non-stationary nanostructure inside the transforming grain embedded in the austenitic matrix is determined. Some nano-structures differ essentially from the prediction of crystallographic theory. Relationships between the number of twins in grain vs. grain size, and width of twin vs. its length are found. Two unexpected stress-relaxation mechanisms at the boundary of transforming grain are revealed.

Keywords: Martensitic phase transformation; Phase field approach; Interface energy and width; Twinning; Nanostructure

1. Introduction

Martensitic phase transformations play a very important part in materials science, being responsible for formation of unique microstructures, mechanical properties, and material phenomena in steels, shape memory alloys and ceramics. Martensitic phase transformation is a first-order, displacive, and diffusionless transformation. During cooling or mechanical loading, the crystal lattice of the cubic phase, austenite (A), transforms to the lower-symmetry lattice of martensite (M). Due to symmetry of the crystal lattice, there is always a finite number of crystallographically equivalent martensitic variants M_i . The typical microstructure during transformation consists of a fine mixture of martensitic variants and residual austenite. The width of each martensitic variant plate is of the order of magnitude

of several to several tens of nanometers and is determined by the interplay of elastic energy of internal stresses and interfacial energy between both martensite and austenite and martensitic variants. There are a number of continuum theories that determine the parameters of such a nanostructure [1–5], assuming some geometry. Alternatively, a phase-field or Ginzburg–Landau (GL) approach was broadly applied to model the evolution of nanostructure without a priori geometric assumptions [6–13]. However, some basic mechanics and physics are still missing in the phase-field equations. Recently, in [14–16], we developed a sophisticated thermodynamic Gibbs potential that allowed us to describe some conceptually important features of known experimental stress–strain curves for shape-memory alloys, steel, and ceramics. Namely, the transformation strain tensor is independent of temperature (in agreement with crystallographic theory [17]), phase transformation starts at nonzero tangent elastic moduli, temperature dependence of stress hysteresis is controlled and can be negligible, and all thermomechanical properties of A and martensitic variants M_i are introduced into the theory for arbitrary symmetry of M_i . Large-strain formulation and simulations are presented in [18]. The importance of dynamics is demonstrated in [19]. The threshold-type (athermal) interface friction is introduced in [20, 21], which allowed us to describe multiphase stationary microstructures. The interface tension is introduced in [22, 23]. Surface-induced phenomena caused by the reduction in surface energy during transformation are described in [22, 23] and the theory was extended for a microscale in [24].

The evolution of martensitic microstructure is described in terms of the evolution of the n order parameters η_i associated with i^{th} martensitic variant M_i . Each order parameter η_i varies from 0, corresponding to A, to 1, corresponding to M_i . The local Helmholtz free energy depends on the elastic strain tensor, temperature, and all order parameters η_i . In addition to the local contribution, the Helmholtz energy includes a part depending on the gradient of the order parameter $\nabla\eta_i$, which is concentrated at the finite-width interface between phases and reproduces the interface energy. The evolution of the order parameters and multivariant martensitic microstructure is described by n Ginzburg–Landau equations, which represent the linear relationships between

the rate of change of the order parameters, $\dot{\eta}_i$, and generalized thermodynamic forces conjugate to them.

One of the remaining problems is related to the current form of the gradient energy, $\psi^\nabla = \frac{\beta}{2} (\sum_{i=1}^n |\nabla \eta_i|^2)$, where β is the gradient energy coefficient. Since ψ^∇ depends on the single material parameter β only, it is clear that it is impossible to vary the energy E_{MM} of the martensitic variant \mathbf{M}_i – martensitic variant \mathbf{M}_j interface independent of the energy E_{AM} of the austenite \mathbf{A} – martensitic variant \mathbf{M}_i interfaces. In fact, as will be shown below, for neglected coupling with mechanics, $E_{MM} = 0.5 E_{AM}$, while in reality energy E_{AM} is independent of the energy E_{MM} and may be essentially larger. In the current paper, the expression for gradient energy is generalized by adding the products $\nabla \eta_i \cdot \nabla \eta_j$ with an additional material parameter b , which allows us to change the energy of the \mathbf{M}_i – \mathbf{M}_j interface independently of that for \mathbf{A} – \mathbf{M}_i interfaces. This results in more sophisticated GL equations, which become coupled through Laplacian operators, in addition to the usual coupling due to local energy terms. Note that while models with multiple gradient energy parameters had already been introduced for martensitic [14] and ferroelectric transformations [28, 29], they never were applied for study of \mathbf{M}_i – \mathbf{M}_j interface. The finite element method (FEM) approach, algorithm, and subroutines are developed using COMSOL Multiphysics code [25].

Detailed analytical study of the \mathbf{M}_1 – \mathbf{M}_2 interface has been performed in [7, 16, 26] for the case in which it is described by a single-order parameter that has opposite signs for the two variants. Both elastic stresses and surface tension were neglected. Here, we will numerically study the \mathbf{M}_1 – \mathbf{M}_2 interface for cubic to tetragonal transformation, when each variant is described by a separate order parameter and both elastic stresses and surface tension are taken into account. A coupled system of two GL equations and equations of elasticity theory, suggested in [22], are used. Solutions are found in a nanosize slab under stress-free boundary conditions and plane stress formulation. The effect of the material parameter b that changes \mathbf{M}_1 – \mathbf{M}_2 interface energy with respect to \mathbf{A} – \mathbf{M} interface energy is studied in detail, and analytical approximations for \mathbf{M}_1 – \mathbf{M}_2 interface energy and width are obtained. Heterogeneous internal stress fields (both elastic and surface tension) are obtained for the case in which a sharp-interface approach suggests a stress-free solution. For relatively large \mathbf{M}_1 – \mathbf{M}_2 interface energy, barrierless austenite nucleation within the \mathbf{M}_1 – \mathbf{M}_2 interface is obtained in the region of stability of martensite, when temperature reduces to the thermodynamic equilibrium temperature. The width of the austenitic region increases toward the free surface, and triple a junction between austenite and two martensitic variants is observed.

Multivariant nanostructure in a nanograin embedded in austenitic matrix was studied as well. For very large overcooling, it resembles finely twinned structure (in agreement with crystallographic theory [17]). However, the small grain size causes deviation from straight interfaces, the width of martensitic variants varies, and non-complete martensitic variants and broadened interfaces are observed. For smaller overcooling, the nanostructure contains a lot of residual austenite, split \mathbf{M}_1 – \mathbf{M}_2 interfaces and triple junctions, as well as incomplete martensite, and it is much different from the prediction of crystallographic theory. Reduction in martensite–martensite interface energy leads

to reduction in twin width, increase in the number of completed variants, reduction of residual austenite, and to sharper interfaces. Some quantitative characteristics of nanostructure as well as specific stress-relaxation mechanisms are found. The effect of the finite element size on the martensite–martensite interface width and energy is studied, and conditions for mesh-independence of the solution are found. It is demonstrated that when element size exceeds the interface width, the obtained nanostructure differs significantly from the correct solution and leads to a wrong conclusion that it is independent of the \mathbf{M}_1 – \mathbf{M}_2 interface energy.

The obtained results represent a more sophisticated and precise model for coherent solid–solid interface than current phenomenological sharp-interface models reviewed in [5, 27]. Our phase-field solution resolves interface structure and heterogeneities of all fields along and across the interface, exhibits heterogeneous elastic stresses and surface tension, and demonstrates the evolution of the interface structure including splitting the interface into two interfaces and the formation of a triple junction as well as the effect of crossing of a free surface.

The paper is organized as follows. In Section 2, a system of coupled phase-field and elasticity equations is presented and discussed. The numerical procedure is outlined in Section 3. Section 4 contains a description of all our results and concluding remarks are presented in Section 5.

Contractions of tensors $\mathbf{A} = \{A_{ij}\}$ and $\mathbf{B} = \{B_{ji}\}$ over one and two indices are designated as $\mathbf{A} \cdot \mathbf{B} = \{A_{ij}B_{jk}\}$ and $\mathbf{A} : \mathbf{B} = A_{ij}B_{ji}$, correspondingly. The subscript s designates symmetrization of a second-rank tensor; the subscripts e and t are utilized for elastic and transformational contributions to the total strain; \otimes is used for a dyadic product of two vectors; \mathbf{I} is the second-rank unit tensor; and $\hat{\nabla}$ and ∇ designate the gradient operators in the undeformed and deformed states. Some preliminary results have been presented in the short letter [22].

2. System of coupled phase-field and elasticity equations

In this Section, we summarize and discuss the main equations from [22]. The total system of equations is presented in Box 1 for n martensitic variants and specified for 2 variants.

To make the theory from [22] more accessible and to focus on our main problem, we simplify it for small-strain formulation. However, to correctly introduce surface tension we will consider finite displacements and keep some terms, which are usually neglected in small-strain formulation. The motion of the elastic material with phase transformations is described by a vector function $\mathbf{r} = \mathbf{r}(\mathbf{r}_0, t)$, where \mathbf{r}_0 \mathbf{r} are the positions of material points in the undeformed Ω_0 and the deformed Ω states, respectively; and t is the time. Material in the reference configuration is in the austenitic state. We introduce traditional decomposition Eq. (3) of the strain tensor $\boldsymbol{\varepsilon} = (\hat{\nabla} \mathbf{u})_s$ into elastic $\boldsymbol{\varepsilon}_e$ and transformational $\boldsymbol{\varepsilon}_t$ parts, where \mathbf{u} is the displacement vector. Eq. (3) also contains decomposition of strain into volumetric ε_0 and deviatoric \mathbf{e} contributions and an expression for the ratio of the mass density in undeformed ρ_0 and deformed ρ states in terms of volumetric strain ε_0 . Transformation strain $\boldsymbol{\varepsilon}_t$ determines the locally unloaded (i.e.,

stress-free) state of material point. For phase transformation between austenite **A** and the i^{th} martensitic variant **M_i**, the order parameter η_i is unambiguously related to the corresponding transformation strain ε_{ti} , which is determined by crystallography. When the order parameter η_i changes between 0 for **A** and 1 for **M_i**, the transformation strain varies between zero and ε_{ti} . In general, transformation strain ε_i depends on all order parameters η_i and is determined by Eq. (4); a is the material parameter.

The Helmholtz free energy per unit undeformed volume $\psi = \bar{\psi}(\varepsilon_e, \eta_i, \nabla \eta_i, \theta)$, where θ is the temperature, can be presented with the help of kinematic decomposition Eq. (3) and Eq. (4) as $\psi = \bar{\psi}(\varepsilon - \varepsilon_t, \eta_i, \nabla \eta_i, \theta) = \psi(\varepsilon, \eta_i, \nabla \eta_i, \theta)$. That is, it can be expressed in terms of total strain or elastic strain and different functions of the order parameters, which is convenient in transferring some equations from [22]. The Helmholtz free energy consists of four contributions (Eq. (6)): the elastic part $\psi^e(\varepsilon_0, \mathbf{e}, \eta_i, \theta)$, the thermal part ψ^θ that is responsible for the driving force for phase transformation, the thermal part $\frac{\rho_0}{\rho} \psi^\theta$ that is responsible for the barrier between phases, and the gradient energy $\frac{\rho_0}{\rho} \psi^\nabla$. Elastic energy Eq. (7) is accepted in the simplest isotropic form with equal bulk K and shear μ elastic moduli of phases. Since elastic strains are much smaller than the transformational strains, neglecting anisotropy and change in elastic moduli does not change any conclusion. The thermal part of free energy is divided into two components, ψ^θ (Eq. (8)) and $\tilde{\psi}^\theta$ (Eq. (10)), one of them $\tilde{\psi}^\theta$ is multiplied in Eq. (6) by the density ratio ρ_0/ρ (the reason will be discussed below). In Eqs. (8)–(11), θ_e is the thermodynamic equilibrium temperature for stress-free **A** and **M**, θ_c is the critical temperature at which stress-free **A** loses its thermodynamic stability; \bar{A} is the barrier for transformation between martensitic variants, similar to $A_0(\theta_e - \theta_c)$ for austenite – martensite transformation (A_0 is the material parameter); B and C are parameters that do not affect the phase equilibrium or phase transformation conditions but affect the thermodynamic potential at parameters η_i away from both the **A** and **M_i** minima and the minimum-energy paths between the minima. The gradient energy in Eq. (13), in contrast to known publications [6, 13, 18–21], contains the products $b \nabla \eta_i \cdot \nabla \eta_j$ with a material parameter b , which allows us to control the energy and width of the **M_i–M_j** interface independent of those for **A–M_i** interface. Gradient energy depends on two material parameters: β , which is present in all theories, and the new parameter b .

Thermodynamic procedure for the materials with a thermodynamic potential depending on gradient of the order parameters $\nabla \eta_i$ in the deformed state and linear relationships between generalized thermodynamic fluxes $\frac{\partial \eta_i}{\partial t}$ and conjugate forces X_i lead to the expression for the true Cauchy stress tensor σ

$$\sigma = \frac{\partial \psi}{\partial \varepsilon} - \sum_{i=1}^n \frac{\rho}{\rho_0} \left(\nabla \eta_i \otimes \frac{\partial \psi}{\partial \nabla \eta_i} \right)_s \quad (1)$$

and to the generalized Ginzburg–Landau equation

$$\frac{\partial \eta_i}{\partial t} = \chi X_i; \quad X_i = - \frac{\rho}{\rho_0} \frac{\partial \psi}{\partial \eta_i} \Big|_\varepsilon + \nabla \cdot \left(\frac{\rho}{\rho_0} \frac{\partial \psi}{\partial \nabla \eta_i} \right) \quad (2)$$

where χ is the kinetic coefficient, and the derivative $\partial \psi / \partial \eta_i$ is calculated at $\varepsilon = \text{const}$. For the chosen potential, Eq. (1) reduces to Eqs. (15)–(17), in which the stress tensor consists of two parts. The elastic stress σ_e is related to elastic strain by Hooke's law Eq. (16). The second contribution σ_{st} (Eq. (17)) is concentrated at the interface (i.e. it is zero if $\eta_i = 0$ and $\eta_i = 1$) and represents surface tension. There are two reasons for the appearance of the surface tension.

The first is because differentiation of the term $\frac{\rho_0}{\rho} = 1 + \varepsilon_0$ with respect to ε_0 gives 1 and results in the appearance of hydrostatic pressure $\psi^\nabla + \tilde{\psi}_\theta$ even for negligible strain ε_0 . That is why the term $\frac{\rho_0}{\rho} = 1 + \varepsilon_0$, negligible in small-strain theory, is kept as a multiplier for the selected energy contributions. The second reason is the presence of the gradient energy $\psi^\nabla(\nabla \eta_i)$. Note that if the energy ψ^∇ depended on the gradient of η_i in the undeformed state, $\nabla \eta_i$, it would not make a contribution to the surface tension. Thus, again even for neglected strains we have to keep the difference between gradients in deformed and undeformed configurations to reproduce the desired surface tension. The criterion for the correct expression for the surface tension in [22] was that for a single-order parameter it reduces to the biaxial tension along the interface, with the total interface force in each direction equal to the surface tension.

The kinetic Ginzburg–Landau Eqs. (2) for n order parameters reduce to Eqs. (19), which for $b \neq 0$ are coupled through Laplacians in addition to traditional coupling through the local energy terms and transformation strain.

The reason that we keep the term $\frac{\rho_0}{\rho}$, which is usually neglected in small-strain approximation, is the following. We found that the sum of the first three terms in the right-hand side of Eq. (19) (local contribution to the driving force) have similar magnitude but the opposite sign to the terms with Laplacians. Thus, a small difference in any of the terms can lead to significant change in the total driving force. Another important point that follows from Eq. (19) is that surface tension tensor σ_{st} does not appear in the expression for the driving force X_i , which depends on elastic stresses only σ_e . However, surface tension indirectly contributes to X_i by affecting stress distribution.

We have to add traditional equilibrium Eq. (22) to complete the total system of equations. Boundary conditions Eq. (23) for each order parameter correspond to the case in which surface energy for the external surface is independent of η_i – i.e., of phase [22].

Box 1: Problem Formulation

B.1. Kinematics

B.1.1. Decomposition of the strain tensor ε

$$\begin{aligned} \varepsilon &= (\nabla \mathbf{u})_s; \quad \varepsilon = \varepsilon_e + \varepsilon_t; \\ \varepsilon &= \frac{1}{3} \varepsilon_0 \mathbf{I} + \mathbf{e}; \quad \frac{\rho_0}{\rho} = 1 + \varepsilon_0 \end{aligned} \quad (3)$$

B.1.2. Transformation strain ε_t

$$\varepsilon_t = \sum_{k=1}^n \varepsilon_{tk} \varphi(\eta_k) - \sum_{i=1}^{n-1} \sum_{j=i+1}^n \eta_i^2 \eta_j^2 (\eta_i \mathbf{L}_{ij} + \eta_j \mathbf{L}_{ji})$$

$$\mathbf{L}_{ji} = (a-3) \varepsilon_{ii} + 3 \varepsilon_{ij}; \quad (4)$$

$$\varphi(\eta_k) = a \eta_k^2 (1 - \eta_k)^2 + (4 \eta_k^3 - 3 \eta_k^4)$$

For two martensitic variants

$$\varepsilon_t = \varepsilon_{t1} (a \eta_1^2 + (4-2a) \eta_1^3 + (a-3) \eta_1^4 - 3 \eta_1^3 \eta_2^2 - (a-3) \eta_1^2 \eta_2^3) \\ + \varepsilon_{t2} (a \eta_2^2 + (4-2a) \eta_2^3 + (a-3) \eta_2^4 - 3 \eta_2^3 \eta_1^2 - (a-3) \eta_2^2 \eta_1^3) \quad (5)$$

B.2. Helmholtz free energy and its contributions

$$\psi = \psi^e(\varepsilon_0, e, \eta_i, \theta) + \frac{\rho_0}{\rho} \check{\psi}^\theta + \psi^\theta + \frac{\rho_0}{\rho} \psi^\nabla \quad (6)$$

B.2.1. Elastic energy for equal elastic properties of phases

$$\psi^e = \frac{1}{2} K \varepsilon_{0e}^2 + \mu \mathbf{e}_e : \mathbf{e}_e \quad (7)$$

B.2.2. The thermal part of the Helmholtz free energy responsible for the driving force for phase transformation

$$\psi^\theta = \frac{1}{3} A_0 (\theta - \theta_c) \sum_{k=1}^n \eta_k^2 (3 - 2 \eta_k) - A_0 (\theta - \theta_c) \sum_{i=1}^{n-1} \sum_{j=i+1}^n \eta_i^2 \eta_j^2 (\eta_i + \eta_j) \quad (8)$$

For two martensitic variants

$$\psi^\theta = \frac{1}{3} A_0 (\theta - \theta_c) \times \{ \eta_1^2 (3 - 2 \eta_1) + \eta_2^2 (3 - 2 \eta_2) - 3 \eta_1^2 \eta_2^2 (\eta_1 + \eta_2) \} \quad (9)$$

B.2.3. The thermal part of the Helmholtz free energy responsible for the barrier between phases

$$\check{\psi}^\theta = \sum_{k=1}^n A_0 (\theta_c - \theta_c) \eta_k^2 (1 - \eta_k)^2 + \sum_{i=1}^{n-1} \sum_{j=i+1}^n F_{ij}(\eta_i, \eta_j) \quad (10)$$

$$F_{ij}(\eta_i, \eta_j) = \eta_i \eta_j (1 - \eta_i - \eta_j) \times \{ B[(\eta_i - \eta_j)^2 - \eta_i - \eta_j] + C \eta_i \eta_j \} + \eta_i^2 \eta_j^2 (\eta_i + \eta_j) (\bar{A} - A_0 (\theta_c - \theta_c)) \quad (11)$$

For two martensitic variants

$$\check{\psi}^\theta = A_0 (\theta_c - \theta_c) \{ \eta_1^2 (1 - \eta_1)^2 + \eta_2^2 (1 - \eta_2)^2 \} + \eta_1 \eta_2 (1 - \eta_1 - \eta_2) \times \{ B[(\eta_1 - \eta_2)^2 - \eta_1 - \eta_2] + C \eta_1 \eta_2 \} + \eta_1^2 \eta_2^2 (\eta_1 + \eta_2) (\bar{A} - A_0 (\theta_c - \theta_c)) \quad (12)$$

B.2.4. Gradient energy

$$\psi^\nabla = \frac{\beta}{2} \left(\sum_{i=1}^n |\nabla \eta_i|^2 + b \sum_{i=1}^n \sum_{j=1, i \neq j}^n \nabla \eta_i \cdot \nabla \eta_j \right) \quad (13)$$

For two martensitic variants

$$\psi^\nabla = \frac{\beta}{2} (|\nabla \eta_1|^2 + |\nabla \eta_2|^2 + 2b \nabla \eta_1 \cdot \nabla \eta_2) = \frac{\beta}{2} (|\nabla \eta_1 + \nabla \eta_2|^2 + 2(b-1) \nabla \eta_1 \cdot \nabla \eta_2) \quad (14)$$

B.3. Stress tensor

$$\boldsymbol{\sigma} = \boldsymbol{\sigma}_e + \boldsymbol{\sigma}_{st} \quad (15)$$

B.3.1. Hook's law for elastic stresses

$$\boldsymbol{\sigma}_e = \frac{\partial \psi^e}{\partial \varepsilon} = K \varepsilon_{0e} \mathbf{I} + 2 \mu \mathbf{e}_e \quad (16)$$

B.3.2. Interface tension tensor

$$\boldsymbol{\sigma}_{st} = (\psi^\nabla + \check{\psi}^\theta) \mathbf{I} - \beta \sum_{i=1}^n (\nabla \eta_i \otimes \nabla \eta_i + b \nabla \eta_i \otimes \sum_{j=1, i \neq j}^n \nabla \eta_j) \quad (17)$$

For two martensitic variants

$$\boldsymbol{\sigma}_{st} = \left[\frac{\beta}{2} ((\nabla \eta_1 + \nabla \eta_2)^2 + 2(b-1) \nabla \eta_1 \cdot \nabla \eta_2) + A_0 (\theta_c - \theta_c) \{ \eta_1^2 (1 - \eta_1)^2 + \eta_2^2 (1 - \eta_2)^2 \} + \eta_1 \eta_2 (1 - \eta_1 - \eta_2) \times \{ B[(\eta_1 - \eta_2)^2 - \eta_1 - \eta_2] + C \eta_1 \eta_2 \} + \eta_1^2 \eta_2^2 (\eta_1 + \eta_2) (\bar{A} - A_0 (\theta_c - \theta_c)) \right] \mathbf{I} - \beta \{ \nabla \eta_1 \otimes \nabla \eta_1 + \nabla \eta_2 \otimes \nabla \eta_2 + b (\nabla \eta_1 \otimes \nabla \eta_2 + \nabla \eta_2 \otimes \nabla \eta_1) \} \quad (18)$$

B.4. Ginzburg–Landau equation

$$\frac{1}{\chi} \frac{\partial \eta_i}{\partial t} = \frac{\rho}{\rho_0} \sigma_e : \frac{d\epsilon_t}{d\eta_i} - \frac{\rho}{\rho_0} \frac{\partial \psi^0}{\partial \eta_i} - \frac{\partial \psi^0}{\partial \eta_i} + \beta(\nabla^2 \eta_i + b \sum_{j=1, i \neq j}^n \nabla^2 \eta_j), \quad i = 1, \dots, n \quad (19)$$

For two martensitic variants

$$\begin{aligned} \frac{1}{\chi} \frac{\partial \eta_1}{\partial t} = \frac{\rho}{\rho_0} \left\{ \{2a\eta_1 + 3(4 - 2a)\eta_1^2 + 4(a - 3)\eta_1^3 \right. \\ \left. - 2(a - 3)\eta_1\eta_2^3 - 9\eta_1^2\eta_2^2\} \sigma_e : \epsilon_{t1} \right. \\ \left. + \{6\eta_1\eta_2^3 + 3(a - 3)\eta_1^2\eta_2^2\} \sigma_e : \epsilon_{t2} \right\} \\ - \frac{\rho}{\rho_0} \frac{1}{3} A_0(\theta - \theta_e) \\ \times \{6\eta_1(1 - \eta_1) + 2\eta_1\eta_2^2(1.5\eta_1 + \eta_2)\} \\ + \eta_1\eta_2(1 - \eta_1 - \eta_2) \{B(2(\eta_1 - \eta_2) - 1) + D\eta_2\} \\ + 2\eta_1\eta_2^2(1.5\eta_1 + \eta_2) (\bar{A} - A_0(\theta_e - \theta_c)) \\ + \beta(\nabla^2 \eta_1 + b\nabla^2 \eta_2) \end{aligned} \quad (20)$$

$$\begin{aligned} \frac{1}{\chi} \frac{\partial \eta_2}{\partial t} = \frac{\rho}{\rho_0} \left\{ \{2a\eta_2 + 3(4 - 2a)\eta_2^2 + 4(a - 3)\eta_2^3 \right. \\ \left. - 2(a - 3)\eta_2\eta_1^3 - 9\eta_2^2\eta_1^2\} \sigma_e : \epsilon_{t2} \right. \\ \left. + \{6\eta_2\eta_1^3 + 3(a - 3)\eta_2^2\eta_1^2\} \sigma_e : \epsilon_{t1} \right\} \\ - \frac{\rho}{\rho_0} \frac{1}{3} A_0(\theta - \theta_e) \\ \times \{6\eta_2(1 - \eta_2) + 2\eta_2\eta_1^2(1.5\eta_2 + \eta_1)\} \\ + \eta_2\eta_1(1 - \eta_2 - \eta_1) \{B(2(\eta_2 - \eta_1) - 1) + D\eta_1\} \\ + 2\eta_2\eta_1^2(1.5\eta_2 + \eta_1) (\bar{A} - A_0(\theta_e - \theta_c)) \\ + \beta(\nabla^2 \eta_2 + b\nabla^2 \eta_1) \end{aligned} \quad (21)$$

B.5. Equilibrium equation

$$\nabla \cdot \sigma = 0 \quad (22)$$

B.6. Boundary conditions for the order parameters

$$n \cdot \nabla \eta_i = 0, \quad i = 1, \dots, n \quad (23)$$

3. Numerical procedure

Material parameters. We will consider cubic-to-tetragonal phase transformation in NiAl alloy. We will use the following material parameters determined and/or collected from the literature in [15, 16, 21, 30]:

$$A_0 = 4.40 \text{ MPa K}^{-1}, \quad \bar{A} = 5.32 \text{ GPa}, \quad \theta_e = 215 \text{ K}$$

$$\theta_c = -183 \text{ K}, \quad a = 2.98, \quad B = 0, \quad D = 0.5 \text{ GPa}$$

$$\beta = 5.18 \cdot 10^{-10} \text{ N}, \quad \chi = 2600 \text{ (Pa} \cdot \text{s)}^{-1} \quad (24)$$

$$K = 112.62 \text{ GPa}, \quad \mu = 71.5 \text{ GPa}$$

In our plane stress 2-D FEM simulations, we included two of the three possible martensitic variants with the following transformation strains [15, 31]: $\epsilon_{t1} = (0.215; -0.078; -0.078)$, $\epsilon_{t2} = (-0.078; 0.215; -0.078)$. Let us determine the range of variation of parameter b from the condition $\psi^\nabla \geq 0$ for all arguments in Eq. (14). It is clear that at the \mathbf{M}_i – \mathbf{M}_j interface one has $\nabla \eta_i \cdot \nabla \eta_j \leq 0$, because for transition from $\eta_i = 1$ and $\eta_j = 0$ to $\eta_i = 0$ and $\eta_j = 1$ across an interface, η_i reduces and η_j increases. Since we can choose $\nabla \eta_i$ arbitrarily to ensure that $\psi^\nabla \geq 0$ for all arguments, we choose $\nabla \eta_i = -\nabla \eta_j$. Then, one has $\psi^\nabla = -\beta(b - 1) |\nabla \eta_i|^2$ and condition $\psi^\nabla \geq 0$ implies $b \leq 1$. Note that for $b = 1$, a sharp-interface solution with $\nabla \eta_i = -\nabla \eta_j$ is $\eta_i = H(\xi)$, which gives zero energy ψ . Here H is the Heavyside step function and ξ is the local coordinate along the normal to an interface with $\xi = 0$ at the interface. Indeed, $\psi^\nabla = 0$ because of $b = 1$, and all other energy contributions, being finite at any point, produce zero interface energy due to zero interface width. Thus, for the thermodynamic parameters for which martensitic variants are stable or metastable, for $b = 1$ the sharp \mathbf{M}_i – \mathbf{M}_j interface represents the minimum interface energy solution. Numerical results below confirm that with $b \rightarrow 1$ the width and energy of the \mathbf{M}_i – \mathbf{M}_j interface tends to zero. We will focus below on the case $b \geq 0$ for which the energy of the \mathbf{M}_i – \mathbf{M}_j interface is less than or equal to the doubled energy of the \mathbf{A} – \mathbf{M} interface.

In the current study, the FEM is utilized, which is implemented in COMSOL code using the arbitrary Lagrangian–Eulerian approach [25]. The complete system of equations describing the phase transformation has a similar mathematical structure to the coupled equations of diffusion and elasticity (or thermoelasticity). The order parameters can be treated as concentrations of different species; ϵ_t is a counterpart of concentration strain with sophisticated dependence on concentrations; Ginzburg–Landau equations are similar to diffusion equations with complex stress- and concentration-dependent sources $-\frac{\rho}{\rho_0} \frac{\partial \psi}{\partial \eta_i}$ and cross-effect

between diffusion of different species in Fick's law. Thus, the GL equations are programmed and solved using Transient Diffusion equations in deformed configuration. Elasticity equations are solved with the help of a Structural Application module. Triangle Lagrange elements with quadratic approximation of the displacements and order parameters have been used. Since for η_i corresponding to \mathbf{A} and \mathbf{M}_i extrema $\partial \eta_i / \partial t = 0$ according to GL Eq. (21), we always include in

the initial condition small deviations from these extrema to avoid a stacking system in them.

We will determine below the width $\Delta_{MM}(0) = 2.07$ nm and energy $E_{MM}(0) = 0.5034 \text{ J m}^{-2}$ of \mathbf{M}_i – \mathbf{M}_j interface for $b = 0$. The maximum surface tension stress σ_{st}^y along the \mathbf{M}_i – \mathbf{M}_j interface has an order of magnitude of 1 GPa. Characteristic phase transformation time, $1/(\bar{A}\chi)$, has an order of magnitude of 0.1 ps and time step in our problems is of the order of 10^{-3} ps. All size, stress, energy, and time parameters will be normalized by 2.07 nm, 1 GPa, 0.5034 J m⁻², and 0.1 ps, respectively. Normalized parameters e.g., E will be designated by bars, \bar{E} . Temperature is uniform and constant for all calculations. The thermal driving force for phase transformation will be characterized by dimensionless overcooling $\bar{\Delta}\theta = \frac{\theta_e - \theta}{\theta_e}$.

To test the numerical procedure, plane vertical interface propagation was considered in a rectangular sample of the size of 8.12×2.71 . Good correspondence with analytical solutions in [14–16, 21] was found. To reduce internal stresses and to check the effect of the external stresses, the following components of the transformation strain have been used: along the vertical interface $\varepsilon_1^y = 0$; normal to the interface $\varepsilon_1^x = 0.05$; and shear-strain $\gamma_1 = 0.1$. For example, for temperature $\theta = \theta_e = 215$ K, normal $\sigma_x = 1$ GPa, and shear stress $\tau = -0.3$ GPa the interface velocity is 993.4 m s^{-1} in our calculations and 998.0 in [21].

To verify the A–M energy, a plane vertical interface propagation was considered in a square sample of the size of 4.83×4.83 . The first martensitic variant is considered only – i.e. $\eta_2 = 0$. To reduce internal stresses at the vertical

A–M interface, crystal lattice of \mathbf{M} is rotated by 36.5° in the right-hand side of the sample to get $\varepsilon_1^y = 0$. This leads to the components of $\varepsilon_{11}^x = 0.1113$, $\varepsilon_{11}^y = 0$ and $\varepsilon_{11}^{xy} = 0.1305$ in the coordinate system xy . In the left half of the sample, initial conditions $\eta_1 = 0.001$ correspond to \mathbf{A} , and in the right part initial conditions $\eta_1 = 0.999$ correspond to \mathbf{M}_1 . The temperature $\theta = \theta_e = 215$ K and the stress-free boundary conditions are accepted. The energy of the A–M interface is $E = 0.2244 \text{ J m}^{-2}$ and equal to the value 0.2244 obtained with analytical expression from [16].

4. Results

4.1. Description of the problem for martensite–martensite interface

The sample in the initial state has a square shape, with the side of 4.83. In the left half of the sample initial conditions $\eta_1 = 0.999$ and $\eta_2 = 0.001$ correspond to \mathbf{M}_1 , and in the right part initial conditions $\eta_1 = 0.001$ and $\eta_2 = 0.999$ correspond to \mathbf{M}_2 . Small initial deviations for η_i from 0 and 1 were used to avoid possible artificial stacking of the system at \mathbf{M}_i minima (as described above), while for this problem it was not necessary. Crystal lattice of the austenite is rotated by 45° , which leads to the components of $\varepsilon_{11}^x = \varepsilon_{11}^y = \varepsilon_{12}^x = \varepsilon_{12}^y = 0.0685$ and $\varepsilon_{11}^{xy} = -\varepsilon_{22}^{xy} = 0.1465$ in the coordinate system xy . External stresses are absent in the deformed state. To avoid rigid-body motion due to numerical errors, one point of the external surface is completely fixed and another one is fixed in the x direction. Initial conditions for stresses are $\sigma = \sigma_{st}$. Homogeneous stationary temperature $\theta = \theta_e$ is accepted.

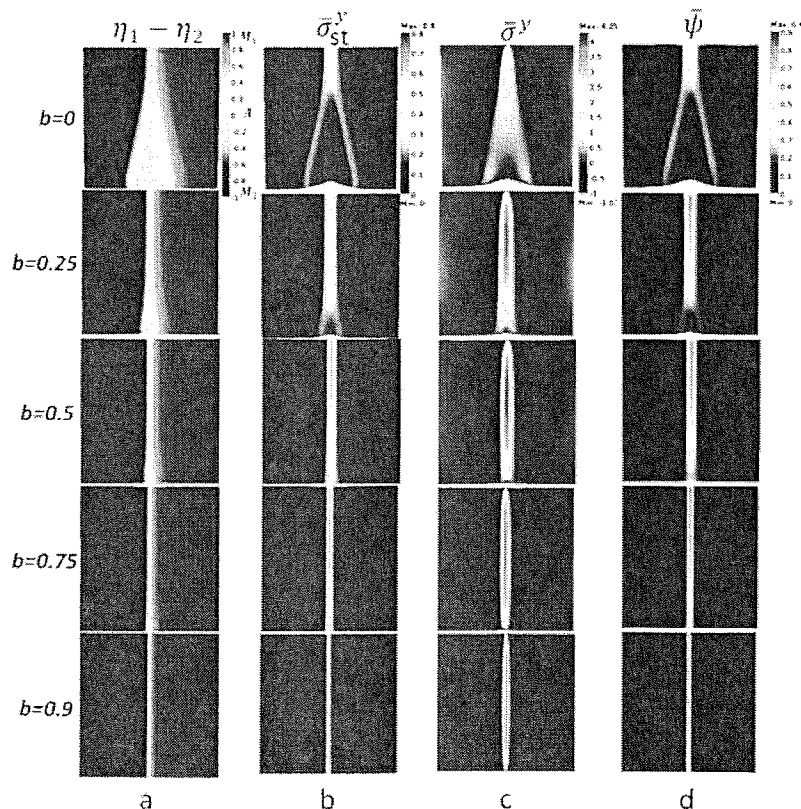


Fig. 1. (a) Distribution of $\eta_1 - \eta_2$, (b) dimensionless surface tension stress $\bar{\sigma}_{st}^y$, (c) total stress $\bar{\sigma}^y$, and (d) energy $\bar{\psi}$ for various parameters b (shown at the left) in a sample with two martensitic variants. For small b , the austenitic region appears at the interface between martensitic variants, leading to splitting of the martensite-martensite interface into two austenite-martensite interfaces and to a triple-junction point.

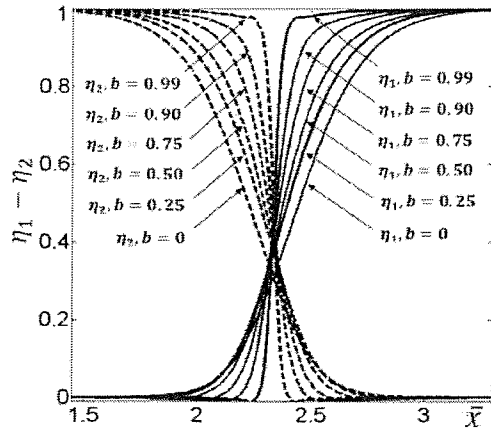


Fig. 2. Profiles of the order parameters η_1 and η_2 vs. \bar{x} at $\bar{y} = 4.35$ for different values of b for the \mathbf{M}_1 – \mathbf{M}_2 interface.

4.2. Martensite-martensite interface contours and width

Profiles of the order parameters η_1 and η_2 vs. \bar{x} at $\bar{y} = 4.35$ are shown in Fig. 2 for different values of b . Isobands of $\eta_1 - \eta_2$ in the sample are presented in Fig. 1a. It is clear that the width of the \mathbf{M}_1 – \mathbf{M}_2 interface decreases with increasing b and decreasing interface energy. For the case $b < 0.8$ – i.e., when the energy E_{MM} of the \mathbf{M}_1 – \mathbf{M}_2 interface is larger than the energy E_{AM} of the \mathbf{A} – \mathbf{M} interface, the austenitic region nucleates barrierlessly at the martensite–martensite interface at the bottom part of a sample; the smaller b is, the larger is the austenitic region. Such a nucleation does not require thermal fluctuations and is observed experimentally e.g., in [32]. Barrierless austenite nucleation within the \mathbf{M}_1 – \mathbf{M}_2 interface starts in the region of stability of martensite ($\theta > \theta_c$), when temperature reduces to the thermodynamic equilibrium temperature. Note that similar nucleation was found in 1-D models with a single-order parameter [16, 26] (so-called soliton splitting). However, in [16, 26] martensitic variants were always separated by the point $\eta = 0$ corresponding to austenite, which expanded into the finite region while approaching the thermodynamic equilibrium temperature. In the current 2-D simulations with two order parameters, one martensitic variant can transform into another without passing through the austenitic point $\eta_1 = \eta_2 = 0$, but still the finite austenitic region $\eta_1 = \eta_2 = 0$ appears between martensitic variants near one of the free surfaces. Also, 2-D simulations exhibited the variable width of the austenitic region and triple junction between an austenite and two martensitic variants. Note that the appearance of an additional phase inside the interface was suggested and explored in the theory of phase transformation via virtual melting [33, 34], in which a molten layer appears at the interface between two solid phases.

There are different ways to define quantitatively the interface width even for a single-order parameter [16, 26]; it is not trivial to do this for two order parameters using interface profiles η_1 and η_2 vs. x . Also, interface width determined with the help of $\eta_1(x)$ and $\eta_2(x)$ profiles is not physical because interface width determined using $\varepsilon_i(x)$ (which is a potentially measured physical parameter) differs significantly. Since transition from \mathbf{M}_1 to \mathbf{M}_2 occurs by a twin-

ning shear along the interface, we use a profile of the shear component

$$\begin{aligned} \varepsilon_i^{xy} = & 0.1465 \{ (a\eta_1^2 + (4-2a)\eta_1^3 + (a-3)\eta_1^4 - 3\eta_1^3\eta_2^2 \\ & - (a-3)\eta_1^2\eta_2^3) - \{ (a\eta_2^2 + (4-2a)\eta_2^3 \\ & + (a-3)\eta_2^4 - 3\eta_2^3\eta_1^2 - (a-3)\eta_2^2\eta_1^3) \} \end{aligned} \quad (25)$$

to determine the martensite-martensite interface width Δ_{MM} (Fig. 3). Thus, $\Delta_{\text{MM}}(b)$ is defined as a length along which transformation shear varies between -0.99 and 0.99 of its maximum magnitude at $\bar{y} = 4.35$, where width and interface energy belong to the region of their small variation along the y direction. For $b = 0$, we obtained $\Delta_{\text{MM}} = 2.07$ nm, which is used as a parameter for normalization of all spatial dimensions. Since $\Delta_{\text{MM}}(0) = s\sqrt{\beta}$ with some parameter s [16], we obtain from our simulations that $s = 9.095 \cdot 10^4 \text{ nm N}^{-0.5}$. Dimensionless interface width $\bar{\Delta}_{\text{MM}}$ vs. b is presented in Fig. 4. Approximation of this curve gives the following equation for the interface width

$$\Delta_{\text{MM}} = 9.095 \cdot 10^4 \sqrt{\beta} (1 - b^{1.445})^{1/2} \quad (26)$$

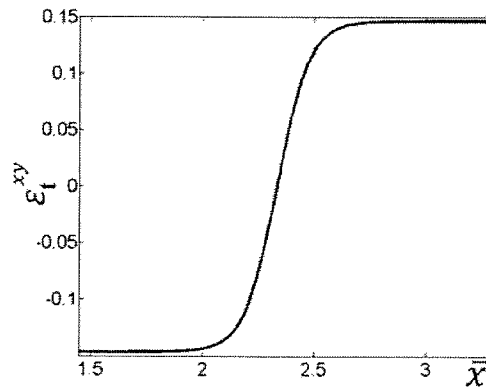


Fig. 3. Distribution of the shear component of the transformation strain along x for $b = 0.5$ at $\bar{y} = 3.86$, which is used for definition of the martensite–martensite interface width.

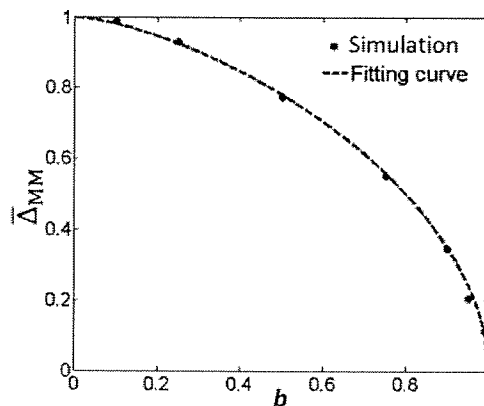


Fig. 4. Dimensionless martensite–martensite interface width $\bar{\Delta}_{\text{MM}}$ vs. b .

4.3. Martensite–martensite interface energy

Energy of a thermodynamically equilibrium interface between phases for arbitrary y is defined as an excess energy with respect to bulk phases, i.e.

$$E := \int_0^l \psi \, dx_0 - \psi_b l \quad (27)$$

where l is the initial width of a sample and integration is performed in an undeformed state. Parameters for the bulk phases (designated with the subscript b) can be taken at the points away from the interface, assuming that they are distributed almost homogeneously and are the same from both sides, which is the case for the examples in the current paper. A more complex situation will be considered elsewhere. We defined E_{MM} for $\bar{y} = 4.35$, which belongs to the region with almost homogeneous energy distribution along the y axis for all b . For $b = 0$ and neglecting internal stresses we obtained $E_{MM} = 0.4490 \text{ J m}^{-2}$, which is twice of the energy of $A-M$ interface. With elastic stresses we have $E_{MM} = 0.5034 \text{ J m}^{-2}$. All energies are normalized by this value. Since $E_{MM}(0) = z\sqrt{\beta}$, with some parameters z [16], we obtain from our simulations that $z = 2.212 \cdot 10^4$. Dimensionless energy of the M_1-M_2 interface \bar{E}_{MM} vs. b , as well as each energy contribution, are presented in Fig. 5. Approximation of this curve gives the following equation for the interface energy

$$E_{MM} = 2.212 \cdot 10^4 \sqrt{\beta} (1 - b^{1.445})^{1/2} \quad (28)$$

It follows from Eqs. (26) and (28) that

$$E_{MM}(b) = 0.24322 \Delta_{MM}(b) \quad (29)$$

i.e., energy of the interface is proportional to its width for all b and the ratio $E_{MM}(b)/\Delta_{MM}(b)$ is independent of b .

Note that for the equilibrium $A-M$ interface described by a single-order parameter and neglected mechanics, analytical solutions give $\psi^\theta = \psi^\nabla$ at each local point [16, 26] (note that $\psi^\theta(\theta_c) = 0$). In our FEM simulations, while total interface energy $E_{AM} = 0.2245 \text{ J m}^{-2}$ coincides with the analytical expression from [16], the contribution of the gradient energy $E_{AM}^\nabla = 0.1149 \text{ J m}^{-2}$ is larger than the contribution of the thermal energy $E_{AM}^\theta = 0.1094 \text{ J m}^{-2}$; elastic energy $E_{AM}^e = 0.0002 \text{ J m}^{-2}$ is negligible. In contrast, for the M_1-M_2 interface described by two order parameters, the contribution E_{MM}^∇ of the gradient energy $\frac{\rho_0}{\rho} \psi^\nabla$ to the

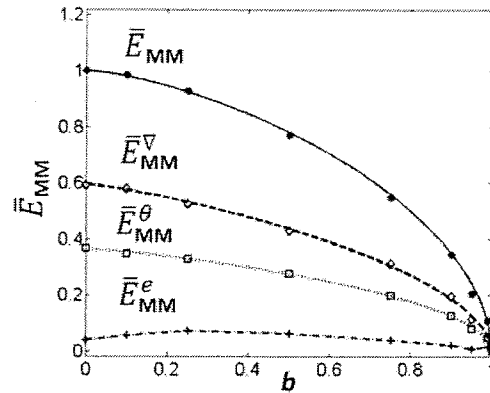


Fig. 5. Dimensionless total energy of the M_1-M_2 interface \bar{E}_{MM} vs. b , as well as each energy contribution due to gradient \bar{E}_{MM}^∇ , thermal \bar{E}_{MM}^θ , and elastic \bar{E}_{MM}^e energies.

E_{MM} is essentially larger than the contribution E_{MM}^θ of the thermal energy $\frac{\rho_0}{\rho} \psi^\theta$ (Fig. 5). Thus, local equality cannot be valid as well. Approximation of the results of the calculation gives

$$E_{MM}^\nabla = 1.316 \cdot 10^4 \sqrt{\beta} (1 - b^{1.220})^{1/2} \quad (30)$$

$$E_{MM}^\theta = 0.8073 \cdot 10^4 \sqrt{\beta} (1 - b^{1.226})^{1/2}$$

For sharp-interface between twins, elastic energy is supposed to be zero (we obtained this using FEM as well). However, for finite-width interface, elastic energy produces a contribution of 4.0 % for $b = 0$, 7.1 % for $b = 0.75$, and 14.5 % for $b = 0.99$. Local energy ψ is distributed symmetrically with respect to the y axis with the sharp maximum at $x = 0$ and almost zero value away from the interface (Fig. 1d), because the only possible contribution, elastic energy, is very small outside the interface. For large b , local energy is almost homogeneous along the y axis, with some reduction for small y due to increase in the interface width and tendency to potentially split into two $A-M$ interfaces, but with some concentration at the bottom free surface. For small b , the region with almost homogeneous energy distribution along the y axis reduces with reduction in b . Maximum energy significantly reduces for y near the interface splitting region. After the interface splits into two $A-M$ interfaces, the local energy maximum is shifted to the center of these interfaces.

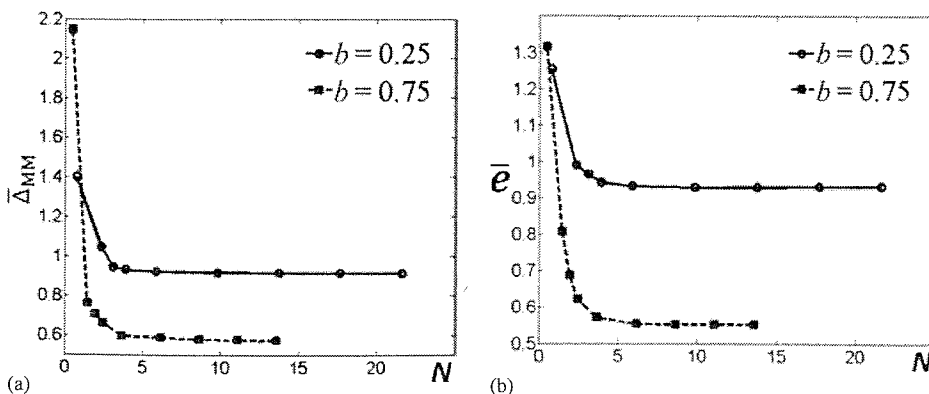


Fig. 6. (a) The M_1-M_2 dimensionless interface width and (b) energy vs. number N of finite elements per interface width (determined by Eq.(26)) for two values of b .

Figure 6 shows the M_1 – M_2 interface width and energy vs. number N of finite elements per interface width (determined by Eq. (26)) for two values of b . It is clear that for more than 6 elements per interface width results are practically independent of the FEM discretization. However, for 3 and fewer elements per interface width, both interface width and energy exceed essentially the correct value, especially for relatively large b . These results allow one to choose proper FEM discretization for the solution of more sophisticated problems with multiple interfaces and complex microstructure and to avoid wrong solutions (see below).

4.4. Martensite–martensite interface tension and stresses

Distributions of total, elastic, and surface tension stresses in the y direction in the entire sample and vs. \bar{x} for $\bar{y} = 4.35$ are shown in Figs. 1 and 7. Note that for sharp-interface and neglected surface tension, total and elastic stresses are zero, which we confirmed by our FEM simulations. In contrast, a finite-width, phase-field solution always results in significant stresses inside and near the interface. Surface tension is localized at the interface and its maximum value increases with growing b . In Fig. 7, the total and elastic stresses are significantly larger than the surface tension; they spread significantly outside of the interface (where they are equal due to the absence of surface tension). Since total force in the y direction should be zero (or within computational error), stresses outside the interface are mostly of the opposite sign to those inside the interface; they have smaller magnitude outside the interface. At the same time, at the external (almost) horizontal surfaces total normal stress is zero due to the boundary condition, and thus the elastic normal stress is equal to minus the normal component of the surface tension. A sharp drop in total stresses

near the intersection of the interface with the free surface of a sample is visible in Fig. 1. In the sharp-interface approach, one would apply concentrated compressive loads equal to the surface tension at the points of intersection of the interface with free surface of a sample. In the phase-field approach there are no external concentrated or distributed loads. Surface tension stress is applied at each point of the interface and zero external normal and shear stresses result in a concentration of elastic stresses and strains in the region where interface crosses the free surface of a sample. For small b , when M_1 – M_2 interface splits into two A – M interfaces, surface tension stress is again localized at the interfaces, while total and elastic stresses spread into the austenitic region. There is no stress concentration at the triple junction point (region).

4.5. Austenite–Martensite interface

The first martensitic variant is considered only – i.e., $\eta_2 = 0$. We start with the rectangular sample of size 4.83×4.83 in the austenitic state. To reduce internal stresses at the vertical A – M interface, a crystal lattice of M is rotated by 36.5° in the right-hand side of the sample to get $\epsilon_t^y = 0$ (Fig. 8) [22]. This leads to the components of $\epsilon_{t1}^y = 0.113$, $\epsilon_{t1}^x = 0$ and $\epsilon_{t1}^{xy} = 0.1305$ in the coordinate system xy . In the left half of the sample initial conditions $\eta_1 = 0.001$ correspond to A and in the right part initial conditions $\eta_1 = 0.999$ correspond to M_1 . When conditions for $\eta_1 = 0.999$ are applied, the right half of the sample deforms to the state shown in Fig. 8. External stresses are absent in the deformed state. To avoid rigid-body motion due to numerical errors, one point of the external surface is completely fixed and another one is fixed in the x direction. Initial conditions for stresses are $\sigma = \sigma_{st}$. Homogeneous stationary temperature is $\theta = \theta_e$. Again, for sharp-interface we ob-

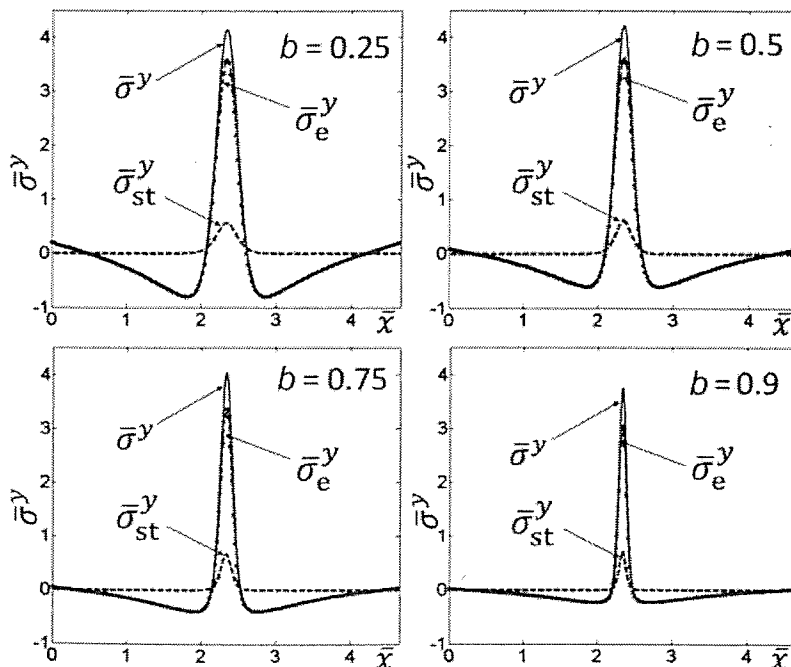


Fig. 7. Distributions of dimensionless total $\bar{\sigma}^y = \bar{\sigma}_{st}^y + \bar{\sigma}_e^y$, elastic $\bar{\sigma}_e^y$, and surface tension stresses $\bar{\sigma}_{st}^y$ in the y direction vs. \bar{x} for $\bar{y} = 4.35$ and several values of b .

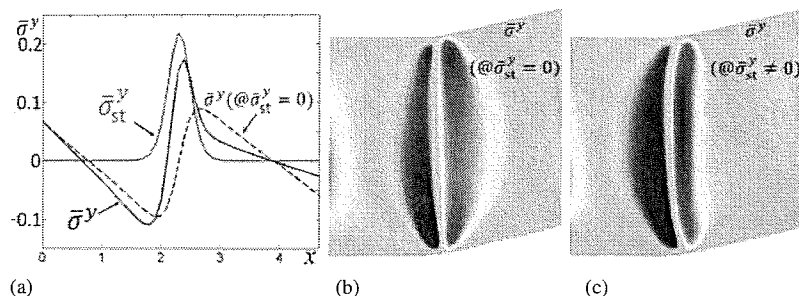


Fig. 8. (a) Plots of the y-component of dimensionless surface tension $\bar{\sigma}_{st}^y$ for the A–M₁ interface, as well as total stress $\bar{\sigma}^y$ for the case with and neglected surface tension stress, along the line passing through the middle of an initially squared sample with a size of 4.83, shown in (b) and (c). Variant M₁ is rotated by 36.5° to get $\varepsilon_{st}^y = 0$ at the A–M₁ interface; (b) and (c) present the distribution of dimensionless total stress $\bar{\sigma}^y$ for the case without and with surface tension, correspondingly.

tained a stress-free solution. For a finite-width interface and $\sigma_{st} = 0$, even while $\varepsilon_{st}^y = 0$ everywhere, there is a significant σ^y stress with concentration near the intersection of the interface and the free surface. Maximum tensile stresses are in the martensite, and compressive stresses are in austenite. The surface tension stress σ_{st}^y exceeds this maximum value of σ^y by a factor of more than 2. Due to asymmetry of the deformed geometry, there is some asymmetry in surface tension distribution. Surface tension changes the distribution of σ^y , increasing significantly the tensile stress and moving its maximum to the center of a sample. The maximum of compressive stress remains near the lower intersection of the interface and the free surface, in the austenitic region. Note that due to the stress-free boundary condition, σ^y is close to zero at the intersection of the interface and the free surface – i.e., stress concentration is shifted inside the sample.

4.6. Martensitic nanostructure formation in the grain

To elucidate the effect of martensite–martensite interface energy and FEM discretization on the nanostructure formation, we consider a square grain with a size of 6.04, in which transformation occurs, embedded in the square matrix with a size of 24.15, which is kept in an austenitic state. The upper and lower external boundaries are fixed in the y direction and free in the x direction. The lower left corner is fixed in the x direction and the vertical sides are stress-free. Displacements are continuous across the surface of the internal square, and the boundary conditions for the or-

der parameters Eq. (23) are applied at this surface. The following initial conditions were applied: all stresses are zero everywhere; in the small square, $\eta_1 = \eta_2 = 0.999$. Since we are interested in a stationary nanostructure, such initial conditions for η_i allowed us to avoid consideration of martensite nucleation and led to fast relaxation to the stationary solution. It is known that small grain size and elastic constraint suppresses martensitic phase transformation [4, 35]. That is why three large overcoolings, $\Delta\bar{\theta} = 1.93$, 2.40, and 4.72, have been studied.

Problems for two different b and two different meshes for each b have been considered: a) for $b = 0.25$ with 11.4 and 2.4 finite elements per interface width determined by Eq. (26); b) for $b = 0.75$ with 9.5 and 1.5 finite elements per interface width – according to Fig. 6, finer mesh should give a mesh-independent solution, but rougher mesh should increase interface width and energy, and solutions may be wrong.

Results of calculations are presented in Fig. 9. First, let us focus on a correct solution for fine mesh. Crystallographic theory and continuum sharp-interface theory suggest an alternate twins solution with planar martensite–martensite interfaces. Results that resemble this solution are obtained under large overcooling only. Small grain size distorts this nanostructure, leading to non-planar interfaces and variable width of martensitic variants, as well as non-complete martensitic variants and broadened interfaces. Most of these distortions are caused by boundary conditions Eq. (23) according to which η_i contour lines should be orthogonal to the sides of an embedded square, which

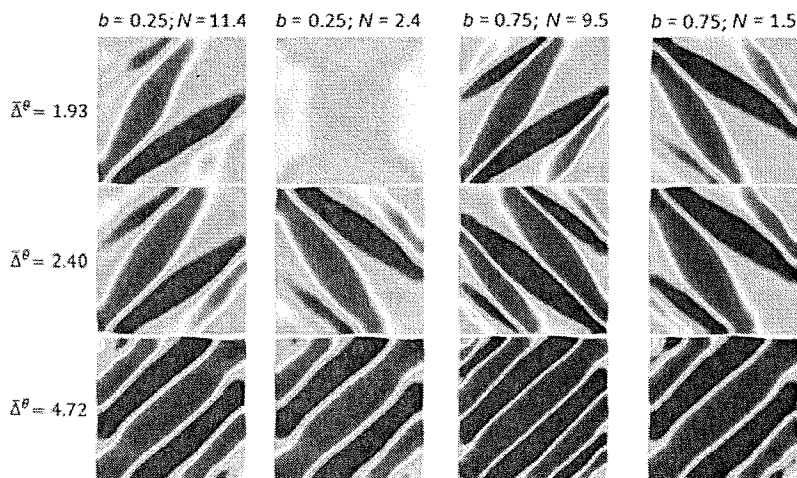


Fig. 9. Stationary distributions of $\eta_1 - \eta_2$ in a square grain with a size of 6.04, in which transformation occurs, embedded in the square matrix with a size of 24.15 (not shown), which is kept in the austenitic state. Results are shown for three different overcoolings $\Delta\bar{\theta} = 1.93$, 2.40, and 4.72 (designated at the left), for two different parameters b and two numbers of finite elements per correct interface width N .

confronts the 45° inclination of martensitic twins that is expected from crystallographic theory. Note that the boundary conditions Eq. (23) mean that the surface energy of the bounding small square is independent of η_i – i.e., of phase state. Also, in the region where twins intersect the square boundary, martensite is not complete (i.e., $\eta_i < 1$), which reduces the energy of internal stresses. Reduction in M_1 – M_2 interface energy leads to the expected reduction in the width of twins and an increased number of twins. For lower overcooling, the nanostructure is much different from the prediction of crystallographic theory. It contains a large number of residual austenite, split martensite–martensite interfaces, and triple junctions, as well as incomplete martensite. Reduction in M_1 – M_2 interface energy leads to an increase in the number of completed twins, reduction of residual austenite, and to sharper interfaces. Note that the residual austenite observed in NiTi shape-memory alloy under conditions when it was completely unexpected [36] can be partially explained by our simulations.

Results for the rough mesh for $b = 0.25$ are completely different from those for the fine mesh for $\Delta\theta = 1.93$; different for $\Delta\theta = 2.40$; and quite close for $\Delta\theta = 4.72$. Results for the rough mesh for $b = 0.75$ show a smaller number of martensitic variants, either incomplete or complete, than with the correct solution for finer mesh. Note that for $\Delta\theta = 4.72$, results for rough mesh for $b = 0.25$ and 0.75 are quite close, while correct solutions for these b 's are dif-

ferent, having different width and number of martensitic variants.

For the mesh with the size of finite element larger than the correct interface width, solutions for some cases became independent of b (Fig. 10). Thus, nanostructures for $b = 0.25$ and $N = 0.95$ and for $b = 0.75$ and $N = 0.60$ are very close for $\Delta\theta = 2.40$ and 4.72 . Nanostructures for $b = 0.25$ and $N = 0.45$ and for $b = 0.75$ and $N = 0.30$ are very close for $\Delta\theta = 1.93$ as well.

To study the scale effect, we consider the same problem but for system size, which is four times larger than in the previous problem – i.e., transforming square grain with the size of 24.15, embedded in the non-transforming austenitic square matrix with the size of 96.62 (see Fig. 11). Mesh-independent solutions for $\Delta\theta = 2.40$ in Figs. 9 and 11 are completely different, with finer nanostructure for a larger sample. Mesh-independent solutions for $\Delta\theta = 2.40$ in Fig. 11 for different b are completely different as well. Thus, in addition to alternating twins structure and chess-board nanostructure [37, 38], novel nontrivial nanostructure is revealed. For larger overcooling $\Delta\theta \geq 3.79$, the solution represents alternating twins for both samples. While the size of a sample increases by a factor of 4, the number of twins increases by a factor of $2 = \sqrt{4}$. Note that usually the width of the twin $w \sim \sqrt{L}$, where L is the size of a sample [37, 39]. Then the number of twins in a sample $n \sim L/w \sim \sqrt{L}$ – i.e., our results correspond to the known relationship. However, in contrast to previous works [37,

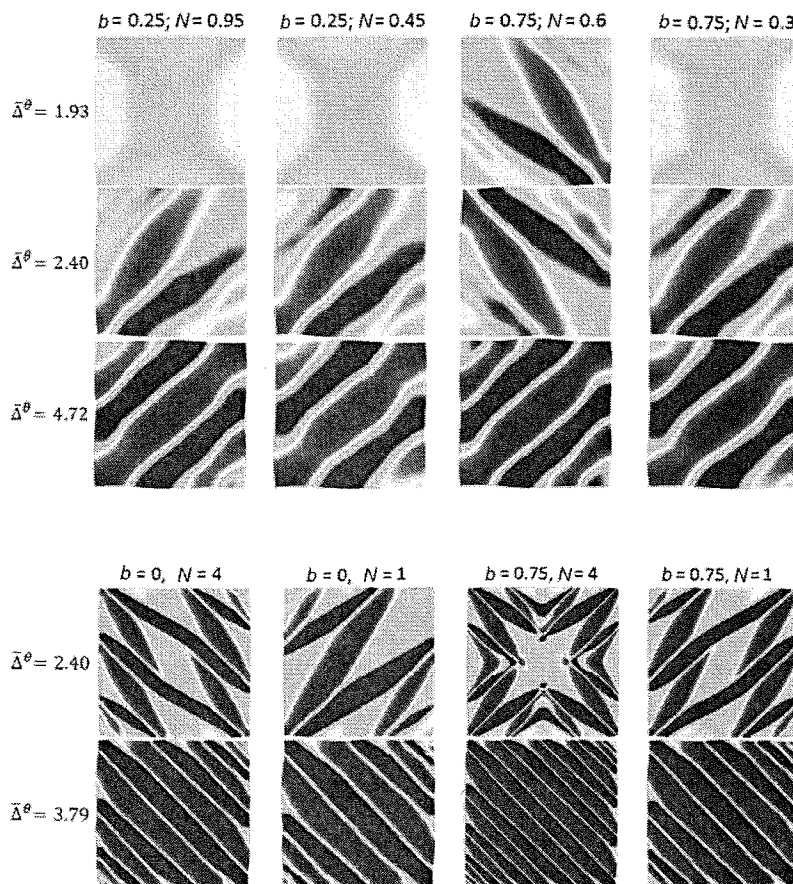


Fig. 10. Mesh-dependent distributions of $\eta_1 - \eta_2$ in a square transforming grain with a size of 6.04, embedded in the square austenitic matrix with a size of 24.15 (not shown). Results are shown for three different overcoolings $\Delta\theta = 1.93$, 2.40 , and 4.72 (designated at the left), for two different parameters b and two numbers of finite elements per correct interface width N .

Fig. 11. Stationary distributions of $\eta_1 - \eta_2$ in a square grain with a size of 24.15, in which transformation occurs, embedded in the square matrix with a size of 96.62 (not shown), which is kept in the austenitic state.

39], the width of the twin w varies within a sample and reduces with reduction of the length of twin l . Figure 12 shows the relationship $w(l)$, which can be approximated as $w = l^{0.38}$. Eqs. (26) and (28) are approximately applicable for the martensite–martensite interfaces in the central region in Figs. 9 and 11 for large overcooling and are not applicable for small overcoolings.

Note that the grain increases its size during transformation, causing compressive stresses from the matrix that suppress martensitic transformation. Fine nanostructure at twinned martensite and grain boundary (Figs. 9, 11, 13)

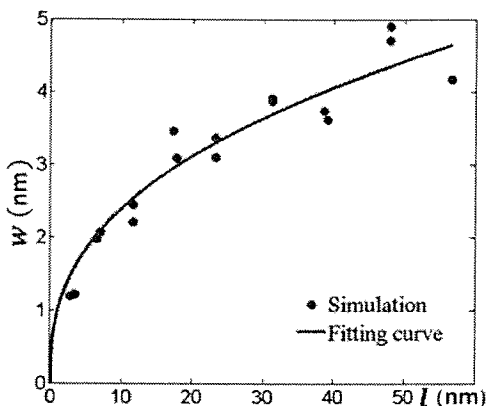


Fig. 12. Relationship between width of the twin w and its length l . Dots are the results of simulation, and the curve is the approximation $w = l^{0.38}$.

contains both convex and concave regions. While concave regions locally reduce expansion of the grain, reducing internal stresses, the convex areas increase grain expansion and internal stresses. Analysis of the nanostructure reveals two stress-relaxation mechanisms at the boundary of transforming grain, as follows.

(a) At relatively large overcooling, leading to an alternate twin structure, incomplete martensite ($\eta_i < 1$) is observed at the intersection of twin and grain boundaries. It appears at locally convex parts of the grain boundary only, where the twin boundary increases internal stresses, and does not appear at the concave part, where the twin reduces size and internal stresses.

(b) At relatively small overcooling, significant residual austenite remains between martensitic variants, and twinned martensite has a relatively small intersection area with grain boundary. It is worth noting that only the concave regions of the intersection of twins and grain boundary are observed.

It follows from Fig. 11 that rough mesh leads to a completely different nanostructure in comparison with fine-mesh solution for $\Delta\bar{\theta} = 2.40$ and to larger twin width for $\Delta\bar{\theta} = 3.79$. Surprisingly, the mesh-independent solutions for $b = 0.75$ are very close to the solutions for rough mesh for $b = 0$. The reason is that if the element size is larger than the correct interface width, it increases interface width and energy and produces a nanostructure corresponding to larger M_i – M_j interface energy – i. e., to smaller b . An example of the nontrivial evolution of the nanostructure with time for a large sample is presented in Fig. 13.

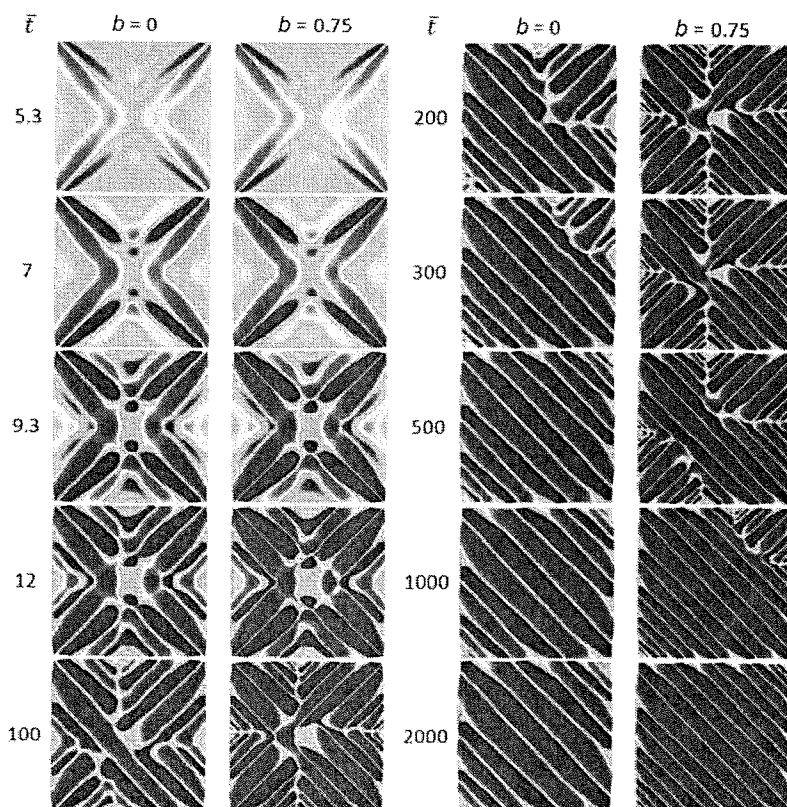


Fig. 13. Evolution of nanostructure leading to the stationary solutions in Fig. 11.

5. Concluding remarks

In summary, phase-field theory for multivariant martensitic phase transformations is extended for the case in which \mathbf{M}_i – \mathbf{M}_j interface energy can be varied independently of the \mathbf{A} – \mathbf{M} interface energy. This has been done by introducing the product of the gradient energy of different order parameters, which results in coupling of the Ginzburg–Landau equations for the order parameters through Laplacians. Surface tension is also taken into account. FEM and COMSOL code have been utilized for the detailed study of the effect of the material parameter b that characterizes \mathbf{M}_i – \mathbf{M}_j interface energy on the solutions and nanostructure evolution. Explicit expressions for \mathbf{M}_i – \mathbf{M}_j interface width and energy are obtained. For relatively large \mathbf{M}_i – \mathbf{M}_j interface energy, martensite–martensite interface splits the producing region of austenite and the triple junction of two martensitic variants and austenite. Such a mechanism of a barrierless austenite nucleation at \mathbf{M}_i – \mathbf{M}_j interface has been observed experimentally, e.g., in [32]. Stationary and non-stationary multivariant nanostructures in a nanograin embedded in austenitic matrix were studied. Only for very high overcooling does it resemble the alternating twin structure predicted by crystallographic theory, but with non-planar interfaces, variable width of martensitic variants, non-complete martensitic variants, and broadened interfaces, caused by the small grain size. For lower overcooling, the nanostructure is much different from the prediction of crystallographic theory. It contains a large amount of residual austenite, split martensite–martensite interfaces, and triple junctions, as well as incomplete martensite. Significant residual austenite between martensitic variants and incomplete martensite at the intersection of twin and grain boundaries (where grain boundary becomes convex) are two main stress-relaxation mechanisms at the boundary of transforming grain. Reduction in the \mathbf{M}_1 – \mathbf{M}_2 interface energy leads to a reduction in the twin width, an increase in the number of completed twins, a reduction of residual austenite, and to sharper interfaces. Relationships between the number of twins in grain and grain size, and between the width of a twin and its length are found. The effect of the finite element size on the \mathbf{M}_1 – \mathbf{M}_2 interface energy and width is studied, and conditions for mesh-independence of the solution are found. Solutions for phase transformation in a nanograin for rough mesh differs significantly from the correct solution for fine mesh. It is demonstrated that when element size exceeds the interface width, the obtained nanostructure is independent of the material parameter b , because \mathbf{M}_1 – \mathbf{M}_2 interface size and energy are determined by the size of the finite element independent of b .

We would like to mention that numerous phenomenological models of coherent interface between phases exist in the literature (see reviews [5, 27]) that are formulated using the theory of thin shell and interface constants that are unknown. In the current work, we obtained a significantly more detailed, flexible, and precise model of a coherent interface, which allows for the non-uniformity of all properties, as well as all types of stresses and strains along the interface and interface thickness. The interface thickness and structure vary during thermomechanical loading. The interfaces can appear and disappear, and they may intersect each other, forming triple-junctions and corner points. While all of these events require separate complex models for the

sharp-interface approach, they can be treated without extra effort in the phase-field approach. Also, no new parameters are required for the interface model that are not involved in the phase-transformation model.

The support of National Science Foundation (CBET-0755236 and CMMI-0969143), the Army Research Office (W911NF-09-1-0001), the Defence Threat Reduction Agency (HDTA1-09-1-0034), and Iowa State University is gratefully acknowledged.

References

- [1] A.L. Roytburd, J. Slutsker: *J. Appl. Phys.* 77 (1995) 2745–2750. DOI:10.1063/1.358744
- [2] H. Petryk, S. Stupkiewicz, G. Maciejewski: *J. Mech. Phys. Solids*. 58 (2010) 373–389. DOI:10.1016/j.jmps.2009.11.004
- [3] H. Petryk, S. Stupkiewicz: *J. Mech. Phys. Solids*. 58 (2010) 390–408. DOI:10.1016/j.jmps.2009.11.003
- [4] T. Waitz, T. Antretter, F.D. Fischer, H.P. Karnthaler: *Mater. Sci. Tech.* 24 (2008) 934–940. DOI:10.1179/174328408X302620
- [5] F.D. Fischer, T. Waitz, D. Vollath, N.K. Simha: *Prog. Mater. Sci.* 53 (2008) 481. DOI:10.1016/j.pmatsci.2007.09.001
- [6] J. Slutsker, A. Artemev, A.L. Roytburd: *Acta Mater.* 52 (2004) 1731. DOI:10.1016/j.actamat.2003.12.015
- [7] G.R. Barsch, J.A. Krumhansl: *Phys. Rev. Lett.* 53 (1984) 1069. DOI:10.1103/PhysRevLett.53.1069
- [8] Y.M. Jin, A. Artemev, A.G. Khachaturyan: *Acta Mater.* 49 (2001) 2309. DOI:10.1016/S1359-6454(01)00108-2
- [9] L.Q. Chen: *Annu. Rev. Mater. Res.* 32 (2002) 113. DOI:10.1146/annurev.matsci.32.112001.132041
- [10] A.E. Jacobs, S.H. Curnoe, R.C. Desai: *Phys. Rev. B* 68 (2003) 224104. DOI:10.1103/PhysRevB.68.224104
- [11] Y.Z. Wang, A.G. Khachaturyan: *Mater. Sci. Eng. A* 55 (2006) 483.
- [12] W. Zhang, Y.M. Jin, A.G. Khachaturyan: *Acta Mater.* 49 (2007) 565. DOI:10.1016/j.actamat.2006.08.050
- [13] T. Lookman, A. Saxena, R.C. Albers: *Phys. Rev. Lett.* 100 (2008) 145504. DOI:10.1103/PhysRevLett.100.145504
- [14] V.I. Levitas, D.L. Preston: *Phys. Rev. B* 66 (2002) 134206. DOI:10.1103/PhysRevB.66.134206
- [15] V.I. Levitas, D.L. Preston: *Phys. Rev. B* 66 (2002) 134207. DOI:10.1103/PhysRevB.66.134207
- [16] V.I. Levitas, D.L. Preston, D.-W. Lee: *Phys. Rev. B* 68 (2003) 134201. DOI:10.1103/PhysRevB.68.134201
- [17] K. Bhattacharya: *Microstructure of Martensite*, University Press Oxford, Oxford (2003).
- [18] V.I. Levitas, V.A. Levin, K.M. Zingerman, E.I. Freiman: *Phys. Rev. Lett.* 103 (2009) 025702. DOI:10.1103/PhysRevLett.103.025702
- [19] A.V. Idesman, J.-Y. Cho, V.I. Levitas: *Appl. Phys. Lett.* 93 (2008) 043102. DOI:10.1063/1.2955514
- [20] V.I. Levitas, D.-W. Lee: *Phys. Rev. Lett.* 99 (2007) 245701. DOI:10.1103/PhysRevLett.99.245701
- [21] V.I. Levitas, D.-W. Lee, D.L. Preston: *Int. J. Plasticity*. 26 (2010) 395–422. DOI:10.1016/j.ijplas.2009.08.003
- [22] V.I. Levitas, M. Javanbakht: *Phys. Rev. Lett.* 105 (2010) 165701. DOI:10.1103/PhysRevLett.105.165701
- [23] V.I. Levitas, K. Samani: *Nature Communications* 2 (2011), 284. DOI:10.1038/ncomm1275
- [24] V.I. Levitas, A.V. Idesman, D.L. Preston: *Phys. Rev. Lett.* 93 (2004) 105701. DOI:10.1103/PhysRevLett.93.105701
- [25] COMSOL, Inc.: website: www.comsol.com.
- [26] F. Falk: *Arch. Mech.* 15 (1983) 63–84.
- [27] H.L. Duan, J. Wang, B.L. Karihaloo: *Adv. Appl. Mech.* 42 (2008) 1. DOI:10.1016/S0065-2156(08)00001-X
- [28] Y.L. Li, S.Y. Hu, L.Q. Chen: *J. Appl. Phys.* 97 (2005) 034112. DOI:10.1063/1.1849820
- [29] J. Hlinka, P. Márton: *Phys. Rev. B* 74 (2006) 104104. DOI:10.1103/PhysRevB.74.104104
- [30] S. Rubini, P. Ballone: *Phys. Rev. B* 48 (1993) 99–111. DOI:10.1103/PhysRevB.48.99
- [31] V.I. Levitas, D.L. Preston: *Phys. Lett. A* 343 (2005) 32–39. DOI:10.1016/j.physleta.2005.05.034
- [32] H. Xu, S. Tan, I. Mueller: *Z. Metallkd.* 89 (1998) 59–64.
- [33] V.I. Levitas: *Phys. Rev. Lett.* 95 (2005) 075701. DOI:10.1103/PhysRevLett.95.075701